Thermal conductivity of metal-organic framework 5 (MOF-5): Part I. Molecular dynamics simulations

B.L. Huang, A.J.H. McGaughey [1], M. Kaviany *

Department of Mechanical Engineering, University of Michigan, 2250 G.G. Brown Laboratory, Ann Arbor, MI 48109-2125, United States

Abstract

The phonon thermal conductivity of MOF-5, a metal-organic framework crystal with a phenylene bridge, is predicted between temperatures of 200 K and 400 K using molecular dynamics simulations and the Green–Kubo method. The simulations are performed using interatomic potentials obtained using *ab initio* calculations and experimental results. The predicted thermal conductivity of MOF-5 is low for a crystal, 0.31 W/m K at a temperature of 300 K, and its temperature dependence is very weak. By decomposing the thermal conductivity into components associated with short- and long-range acoustic phonons, and optical phonons, the weak temperature dependence is found to be related to the mean free path of the majority of phonons, which is of the order of lattice parameter (and is essentially temperature independent). To interpret the results, an analytical thermal conductivity relation is derived, which reduces to the Cahill–Pohl and Slack models under appropriate assumptions. The relation contains a critical frequency, which determines the relative contributions of the short- and long-range acoustic phonons. The small long-range acoustic phonon contribution is found to be related to the long and flexible phenylene bridge, and to the mass mismatch between the cages and the bridges.

Keywords: Metal-organic framework; Molecular dynamics simulations; Thermal conductivity; Nanoporous crystals; Potentials

1. Introduction

The metal-organic frameworks (MOFs), a sub-family of the nanoporous crystals, are characterized by metal-oxygen cages (vertices) connected by organic bridges [1–4]. MOFs currently attract intensive interest for their excellent potential for storing and separating gases (e.g., N_2, Ar, CO_2, CH_4, and H_2) [5–7]. By changing the organic bridge and/or its functionalization, new MOFs can be designed and synthesized without changing the underlying topology. Recent work has focused on their structural properties [2], adsorption characteristics [2,5–7], and the diffusion of light gases through them [8], but their thermal transport characteristics have yet to be considered. Since the gas absorption/desorption is sensitive to the unintended change in the ambient temperature and this response is related to the absorption/desorption bed thermal conductivity, the knowledge of the thermal conductivity of a MOF is crucial in predicting the behavior. Furthermore, the variety of MOFs available points towards the possibility of systematically designing materials with specified thermal properties. To prepare for such molecular design, an understanding of the relationship between a MOF structure and its thermal conductivity is required.

We report the investigation of the thermal transport in MOF-5 (shown in Fig. 1), which is the smallest of a series of MOFs that have a simple cubic crystal structure [2]. It is built from zinc–oxygen tetrahedra connected by 1,4-benzenedicarboxylate (BDC) bridges. It has a low density (610 kg/m³), a large free cage volume (79%), and a pore diameter of 11.2 Å [2].

There are two standard approaches for predicting the thermal conductivity of a solid, both of which are based

---
* Corresponding author. Tel.: +1 734 936 0402; fax: +1 734 647 3170.
E-mail address: kaviany@umich.edu (M. Kaviany).
[1] Present address: Department of Mechanical Engineering, Carnegie Mellon University, Pittsburgh, PA 15213, United States.

Nomenclature

a	mean atomic distance	κ_s	compressibility
b	constant	λ	mean free path
c	concentration	v	Poisson ratio
k	thermal conductivity	ω	angular frequency
n	number density	$\dot{\omega}$	heat current
P	pressure	ρ	density
q	charge	τ	time constant
r	distance	φ	potential energy
t	time		
$\mathbf{u}$	velocity	*Subscripts*	
A	coefficient	A	acoustic
B	coefficient	CP	Cahill–Pohl
D	density of states	i	summation index, particle label
E	energy	j	summation index, particle label
I	spectral density	p	phonon
$\mathbf{M}$	dipole moments	g	group
M	atomic weight	c	cell
N	number of particles	O	optical
N_c	number of atoms in a primitive cell	T	transversal
R_c	cut-off radius	L	longitudinal
T	temperature	D	Debye
V	volume	sh	short-range
		lg	long-range
Greek symbols		κ	wave vector
β	Wolf method parameter	β	species
γ_G	Grüneisen constant		

on the Fourier law. One approach is to use continuum transport theory and kinetic theory, such as the Boltzmann transport equation (BTE) approach of Callaway [9] and Holland [10]. The second is to use an atomistic technique, such as molecular dynamics (MD) simulations. The BTE can be used to study large systems rather quickly, but for a reliable calculation, a good understanding of the underlying phonon processes is required. Parameters such as the phonon relaxation times must be obtained from other approaches (e.g., by fitting to experimental data [9,10] or directly from MD [11]). Molecular dynamics is a more fundamental method, which tracks the positions and momenta of an ensemble of classically interacting atoms. For input, MD only requires a material structure and suitable interatomic potentials. In this investigation, MD will be used to predict the thermal conductivity of MOF-5. The data required for a BTE study is currently unavailable.

We first describe the development of the classical interatomic potentials (force fields) needed to perform MD simulations of MOFs. Using these potentials, the thermal conductivity of MOF-5 is predicted between temperatures of 200 K and 400 K. The thermal conductivity is decomposed into components associated with short- and long-range acoustic phonons and optical phonons. A model is formulated to explain the observed weak temperature dependence, and a critical frequency is introduced to sepa-

rate the contributions of the two acoustic components. Finite size and quantum effects on the thermal conductivity prediction are also discussed. The relationship between the MOF-5 structure and its thermal behavior is explored, and a simplified structural model is proposed.

2. Classical interatomic potentials for MOF-5

To model the dynamics of MOF-5, the development of potentials for different interactions in MOF-5 is required. Previous MD studies have focused on the interaction of gases with the structure, and modeled the crystal as being rigid [8]. The main challenge in the construction of a potential set is related to the oxygen atom in the carboxylate moiety, which has a charge of −0.5. While potentials exist for Zn–O systems with formal charges [12], parameters are not available for this reduced charge state. To construct the potentials, we fit selected algebraic expressions to energy surfaces obtained from *ab initio* calculations.

The *ab initio* calculations are performed with Gaussian 98 [13], which is a software package for electronic structure calculation. First, to determine the appropriate method/ basis set, the MOF-5 structure is relaxed using common combinations, e.g., RHF/6-311g (here RHF is the method and 6-311g is the basis). The resulting structures are then compared to the experimental data, as shown in Table 1.
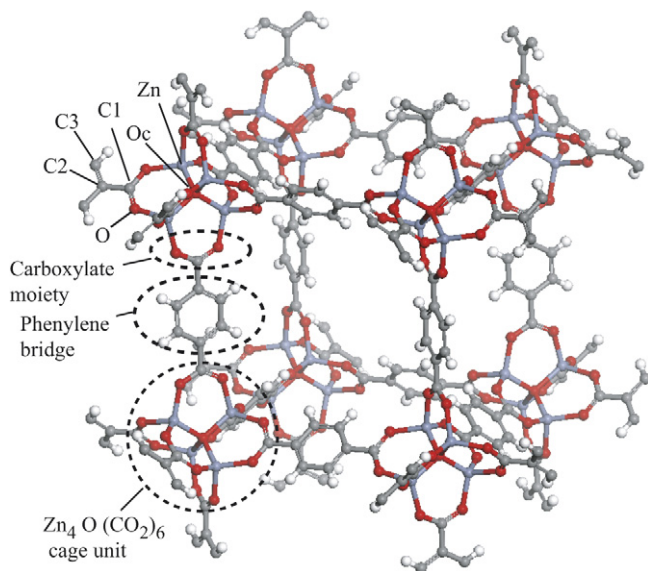
Fig. 1. MOF-5 unit cell: $8[Zn_4O(BDC)_3]$. This is the $1 \times 1 \times 1$ system. The cage is built from four zinc–oxygen tetrahedra ($ZnOcO_3$), which share the Oc atom (located at the center of the cage). The O–C1–O group forms a carboxylate moiety, to which a phenylene group is attached. Note the distinction between the three carbon sites. The carboxylate moieties on either side of a phenylene ring are perpendicular. Thus, eight cages and 12 bridges are required to form the simple cubic unit cell, which has a lattice constant of 25.85 Å. The formal charges on the oxygen atoms at the center of the cage (Oc), the carboxylate-oxygen atoms (O), and the zinc atoms are -2, -0.5, and $+2$. The other species are charge neutral.

Based on a sum of squares error calculation (compared to the experimental data), B3YLP/6-311g** is found to be most suitable. The energy surface of MOF-5 is then scanned using B3YLP/6-311g** by changing bond lengths and angles. The classical potentials are fitted to this data using the general utility lattice program (GULP) [14].

The set of interatomic potentials includes two-body (pair), three-body (angular), and four-body (torsional) terms, as presented in Table 2. The C2 and C3 atoms are treated in the same way in the pair and angular potentials (denoted as C2/3). The C2/3–C2/3–C2/3 bending and C2/3–C2/3–C2/3–C2/3 torsion potentials are taken from Chelli et al. [15]. Other than electrostatics, no two-body

interactions are assumed for the non-bonded pairs of Oc–O, O–O, and Zn–Zn. These interactions are best captured with the three- and four-body potentials. The hydrogen atoms are not directly included in the model. The C3-H group is taken to be a rigid entity (by adding the hydrogen mass to the carbon mass), a common treatment for hydrogen atoms in MD [16].

The MOF-5 structure is then relaxed under the new potentials with GULP. The resulting structural parameters are shown in Fig. 2, where they are compared with the experimental data [17]. The average difference between the predicated data and the experimental data are 2%. The MOF-177, IRMOF-11, and IRMOF-16 structures have also been successfully relaxed in GULP using these potentials, indicating their transferability to other MOFs.

To further validate the potential, we compare the MD predicted infrared (IR) spectrum and that from experimental NIR-FT (Near InfraRed-Fourier Transform) measurements [17]. The range of the NIR-FT data are from 75 Trad/s to 375 Trad/s (400 cm^{-1} ∼ 2000 cm^{-1}). The MD predicted IR spectrum is obtained by taking the Fourier transform of the electrical flux autocorrelation function [18]:

$$I(\omega) \propto \int_0^\infty \left\langle \frac{d\mathbf{M}(t)}{dt} \cdot \frac{d\mathbf{M}(0)}{dt} \right\rangle \cos(\omega t) dt, \quad (1)$$

where

$$\frac{d\mathbf{M}(t)}{dt} = \sum_{i=1}^N q_i \mathbf{u}_i(t). \quad (2)$$

Here, $I(\omega)$ is the spectral density, ω is angular frequency, $\mathbf{M}(t)$ is the summation of the individual dipole moments of all the atoms in the system, t is time, N is the number of atoms in the system, q_i is the charge on the ith atom, and $\mathbf{u}_i(t)$ is the velocity of ith atom. In Fig. 3, the two IR spectra are shown and the main band peaks are identified. There are much more details in the calculated spectrum. The match of the main peaks in the low frequency region (<200 Trad/s) is considered good. The deviation becomes noticeable in the high frequency region ($\geqslant$200 Trad/s). The average deviation between the main band peaks

Table 1
The structural parameters predicted by different *ab initio* methods/basis sets and the experimental data [1]

Method/basis	Bond lengths (Å)					Angles (°)				S^2 (10^{-3})
	Oc–Zn	Zn–O	O–C1	C1–C2	C2–H	Oc–Zn–O	Zn–O–C1	O–C1–C2	C2–C3–H	
RHF/sto-3g*	1.877	1.865	1.281	1.549	1.085	113.5	127.6	116.1	108.8	6.23
RHF/6-311g**	1.992	1.962	1.241	1.504	1.080	109.5	133.6	117.2	108.8	1.53
RHF/6-311+g**	1.996	1.981	1.242	1.506	1.080	109.5	133.3	117.1	108.8	1.95
RHF/LANL2DZ	2.044	1.973	1.271	1.504	1.077	108.9	135.3	119.4	109.1	4.81
B3YLP/6-311g**	**1.972**	**1.953**	**1.262**	**1.510**	**1.088**	**110.8**	**131.7**	**117.8**	**111.1**	**0.76**
B3YLP/6-311+g**	1.982	1.980	1.265	1.512	1.087	110.8	131.6	117.8	111.0	1.40
B3YLP/LANL2DZ	2.037	1.988	1.295	1.514	1.091	110.0	133.6	118.8	110.5	4.92
Experiment	1.936	1.941	1.252	1.498	1.090	111.1	132.3	118.1	109.5	

B3YLP/6-311g** gives the best agreement with the experimental data based on a sum of squares calculation. $S^2 = \sum_{i=1}^9 [(s_i - s_{exp})/s_{exp}]^2$, where the summation is over the bond lengths and angles listed.

Table 2
The interatomic potentials for MOF-5

Interaction	Potential model	Parameters
Pair		
Oc–Zn	$\frac{1}{r}q_{Oc}q_{Zn} + A\exp\left(-\frac{r}{r_o}\right) - Cr^{-6}$	$A = 770.127$ eV, $r_o = 0.357$ Å, $C = 0.00088$ eV Å^6
Oc–O	$\frac{1}{r}q_{Oc}q_O$	
O–Zn	$\frac{1}{r}q_{Oc}q_{Zn} + A\exp(-\frac{r}{r_o}) - Cr^{-6}$	$A = 529.7$ eV, $r_o = 0.352$ Å, $C = 0.0$ eV Å^6
Zn–Zn	$\frac{1}{r}q_{Zn}q_{Zn}$	
O–O	$\frac{1}{r}q_O q_O$	
O–C1	$\varphi_o\{[1 - \exp(-a(r - r_o))]^2 - 1\}$	$\varphi_o = 4.624$ eV, $a = 2.337$ Å^{-1}, $r_o = 1.28$ Å
C1–C2	$\varphi_o\{[1 - \exp(-a(r - r_o))]^2 - 1\}$	$\varphi_o = 5.439$ eV, $a = 1.669$ Å^{-1}, $r_o = 1.482$ Å
C2/3–C2/3	$\varphi_o\{[1 - \exp(-a(r - r_o))]^2 - 1\}$	$\varphi_o = 8.196$ eV, $a = 1.680$ Å^{-1}, $r_o = 1.388$ Å
Angular		
C2/3–C2/3–C2/3	$\frac{1}{2}k_\theta(\cos\theta - \cos\theta_o)^2$	$k_\theta = 11.732$ eV, $\theta_o = 120°$
O–C1–O	$\frac{1}{2}k_\theta(\cos\theta - \cos\theta_o)^2$	$k_\theta = 11.0$ eV, $\theta_o = 120°$
C1–C2–C3	$\frac{1}{2}k_\theta(\cos\theta - \cos\theta_o)^2$	$k_\theta = 9.599$ eV, $\theta_o = 120°$
Zn–O–C1	$\frac{1}{2}k_\theta(\cos\theta - \cos\theta_o)^2$	$k_\theta = 11.0$ eV, $\theta_o = 132.3°$
Torsional		
C2/3–C2/3–C2/3–C2/3	$k_\phi[1 - \cos(\phi - \phi_o)]$	$k_\phi = 1.735$ eV, $\phi_o = 0°$
O–C1–C2–C3	$k_\phi[1 - \cos(\phi - \phi_o)]$	$k_\phi = 1.587$ eV, $\phi_o = 0°$
O–C1–O–Zn	$k_\phi[1 - \cos(\phi - \phi_o)]$	$k_\phi = 1.732$ eV, $\phi_o = 0°$

r, θ and ϕ are distance, bond angle and torsion angle. The C2 and C3 atoms are treated in the same way in the pair and angular potentials (denoted as C2/3). The cutoff radius of electrostatic terms is 10 Å. For all other terms, only bonded interactions are considered.
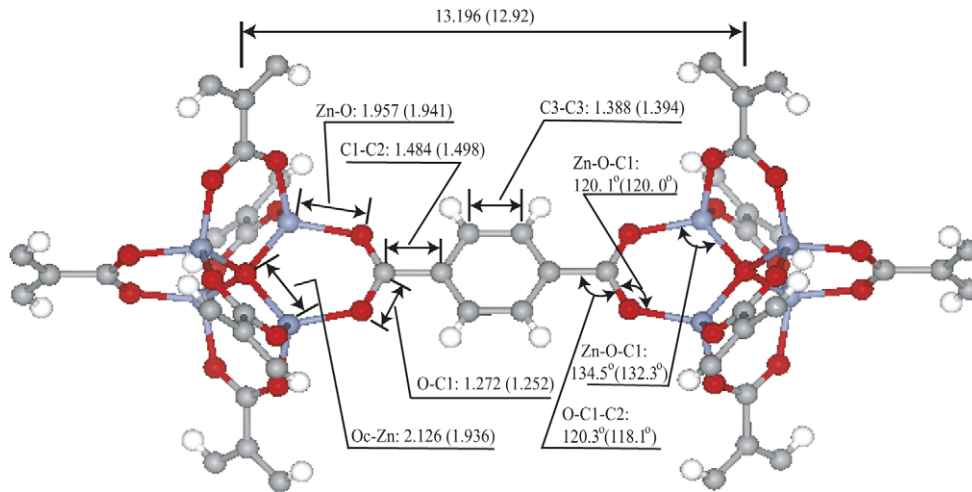

Fig. 2. The MOF-5 structure produced by optimization with GULP using the new potentials and the experimental data (in parentheses). The lengths are in (Å) and the angles are in (°).

predicted by MD and the associated experimental data are 3.5%, which we take to be good agreement [19].

3. Simulation details

3.1. Logistics

All data used for the thermal conductivity predictions come from simulations run in the NVE (constant mass, volume, and energy) ensemble. Unless noted, the simulation cell contains eight unit cells in a $2 \times 2 \times 2$ arrangement (2624 atoms). Size effects will be discussed in Section 3.2. The Verlet leapfrog algorithm is used to integrate the equations of motion with a time step of 0.2 fs.

The Wolf method is applied to model the electrostatic interactions according to [20]:

$$\frac{q_i q_j}{r_{ij}} \simeq \frac{q_i q_j \text{erfc}(\beta r_{ij})}{r_{ij}} - \lim_{r_{ij} \to R_c}\left\{\frac{q_i q_j \text{erfc}(\beta r_{ij})}{r_{ij}}\right\}, \quad (3)$$

where r_{ij}, β, and R_c are the distance between atoms i and j, the damping parameter, and the cut-off radius. The Wolf method can significantly reduce the computation time compared to the traditional Ewald sum. Demontis et al. [21] suggest taking $R_c \geqslant 5b$ and $\beta \simeq 2/R_c$, where b corresponds to the largest of the nearest-neighbor distances between particles of opposite charge. For MOF-5, $b \simeq 2$ Å (see Fig. 2). Thus, we choose R_c to be 10 Å, and β to be 0.2 Å^{-1}. To find the zero-pressure lattice constant as a
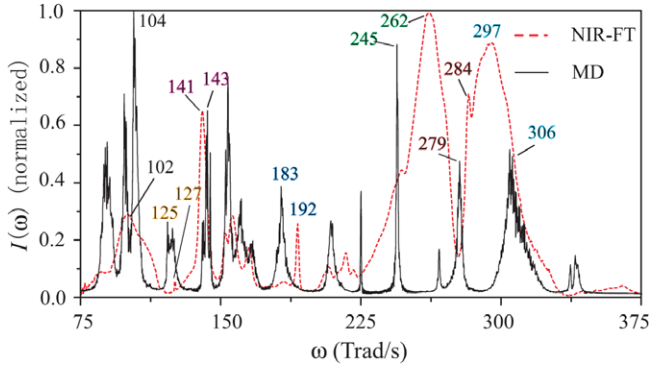
Fig. 3. The IR spectrum calculated from MD and the experimental (NIR-FT) results. The curves are normalized against the largest peak in each data set. The correspondence between peaks is established by comparing the partial density of states of the species calculated from MD (see Fig. 8) to the results of experiments, [17] and by visual comparison of the two spectra. The 127/125 peak is related to vibrations of the Oc atom, the 245/262 peak is associated with symmetric stretching of the carboxylate moiety, the 284/279 peak results from vibrations of the phenylene ring, and the 306/297 peak is associated with asymmetric stretching of the carboxylate moiety.

function temperature, simulations are run in the NPT (constant mass, pressure, and temperature) ensemble, and an average was taken over 20 ps of data. The Nose–Hoover thermostat and the Berendsen barostat are used to control the system temperature and pressure [22].

3.2. Quantum effects

Below the Debye temperature, T_D, phonon mode populations in a quantum system are temperature dependent, but almost temperature independent in a classical system, such as MD [11]. By running the current simulations at temperatures above the Debye temperature, errors that may result from ignoring quantum effects when comparing to experimental data will be minimized.

The Debye temperature for a monatomic crystal is defined as [23]

$$T_D = \frac{\hbar_P}{k_B} u_{p,g} (6\pi^2 n)^{1/3}, \tag{4}$$

where $\hbar_P$ is the Planck constant divided by 2π, k_B is the Boltzmann constant, $u_{p,g}$ is the sound speed (an average phonon group velocity) and n is the atomic number density (N/V). For polyatomic crystals, Slack [24] ignored the optical branches and introduced a factor $1/N_c^{1/3}$ to Eq. (4) (N_c is the number of atoms in the unit cell). For MOF-5, where the mass and bond differences are small among most atoms, the correction to Eq. (4) is expected to be smaller. Using Eq. (4) as given will thus somewhat overestimate the Debye temperature and provide a safe estimate of the temperatures for which the simulations will be comparable to experimental data.

To find the Debye temperature, a sound speed is required, which can be obtained from MD simulations

using the following procedure. In the NVE ensemble, the adiabatic compressibility, κ_s, is given by [25]

$$\kappa_s = \left[\frac{2}{3}P + nk_B T + \left\langle \sum_{i,j} \frac{\partial^2 \varphi}{\partial r_i \partial r_j} \right\rangle - \frac{N}{nk_B T} \langle (\delta P)^2 \rangle \right]^{-1}, \tag{5}$$

where P is the pressure, φ is the total potential energy, and δP is the root-mean-square pressure fluctuation, i.e., $\langle (\delta P)^2 \rangle = \langle (P - \langle P \rangle)^2 \rangle$. At a temperature of 300 K, the adiabatic compressibility is found to be 7.09×10^{-10} Pa^{-1}. With the adiabatic compressibility, the longitudinal sound velocity $u_{p,g,L}$ and transverse sound velocity $u_{p,g,T}$ can be determined from [26,27]

$$u_{p,g,L} = \left[\frac{3(1 - 2v)}{\kappa_s \rho} \right]^{1/2} \tag{6}$$

$$u_{p,g,T} = \left[\frac{3(1 - 2v)}{2(1 + v)\kappa_s \rho} \right]^{1/2}, \tag{7}$$

where ρ is density and v is the Poisson ratio. For most solids, $v \simeq 0.3$. An average sound speed, $u_{p,A}$, can be given by $3u_{p,A}^{-1} = u_{p,g,L}^{-1} + 2u_{p,g,T}^{-1}$, which yields $u_{p,A} = 1184$ m/s for MOF-5 at a temperature of 300 K, a reasonable value. Using Eq. (4) (replacing $u_{p,g}$ with $u_{p,A}$), we have $T_D \simeq 102$ K. We will consider temperatures between 200 K and 400 K (at 50 K intervals), well above the estimated T_D.

3.3. Thermal conductivity prediction

The thermal conductivity, k, is predicted using the Green–Kubo (GK) method, where, for an isotropic material, it is given by [28]

$$k = \frac{1}{k_B V T^2} \int_0^\infty \frac{\langle \dot{\mathbf{w}}(t) \cdot \dot{\mathbf{w}}(0) \rangle}{3}, \tag{8}$$

where $\dot{\mathbf{w}}(t)$ is the heat current vector, and $\langle \dot{\mathbf{w}}(t) \cdot \dot{\mathbf{w}}(0) \rangle$ is the heat current autocorrelation function (HCACF). A slow-decaying HCACF indicates that the heat current fluctuations can spread over a long time before vanishing (i.e., a long phonon relaxation time). The heat current is given by

$$\dot{\mathbf{w}} = \frac{d}{dt} \sum_{i=1}^{N} \mathbf{r}_i E_i, \tag{9}$$

where $\mathbf{r}_i$ and E_i are the position vector and the total energy of particle i. The GK method has been used to investigate the thermal properties of dielectric materials such as diamond [29], silicon [30,31], zeolites [32], and amorphous silicon [33]. This approach is based on fluctuation-dissipation theory and is an equilibrium method. As we believe MOF-5 to be a good dielectric, the electronic component of the thermal conductivity is taken as negligible.

Thermal conductivity can also be predicted in MD using the direct method, which closely resembles an experimental technique based on an application of the Fourier law [30]. The direct method is a steady-state, non-equilibrium method in which a steady 1-D heat flux is imposed on a

system. From the resulting temperature gradient, the thermal conductivity is directly obtained using the Fourier law. The direct method normally has strong non-linear response behavior and significant size effects. Large atomic system are typically required to obtain an accurate prediction of the bulk phase thermal conductivity (it is better suited, in fact, to the study of thin films) [30]. For a complex crystal with a large unit cell (such as MOF-5), the computational demands would be tremendous. The linear response behavior of the GK method leads to accurate results using smaller atomic system than required in the direct method [30]. The GK method is also advantageous as it allows for the decomposition of the thermal conductivity into contributions associated with acoustic and optical phonons [32].

At the beginning of a simulation for a thermal conductivity prediction, the system is run in the NVT ensemble to set the temperature. After 20 ps, when the system has reached equilibrium, the simulation is switched to run in the NVE ensemble, and the HCACF is obtained over 200 ps. At each temperature, three runs are performed unless noted. The thermal conductivity is then obtained from the integral of the HCACF [32]. A running average is applied to the integral to obtain a smooth behavior,
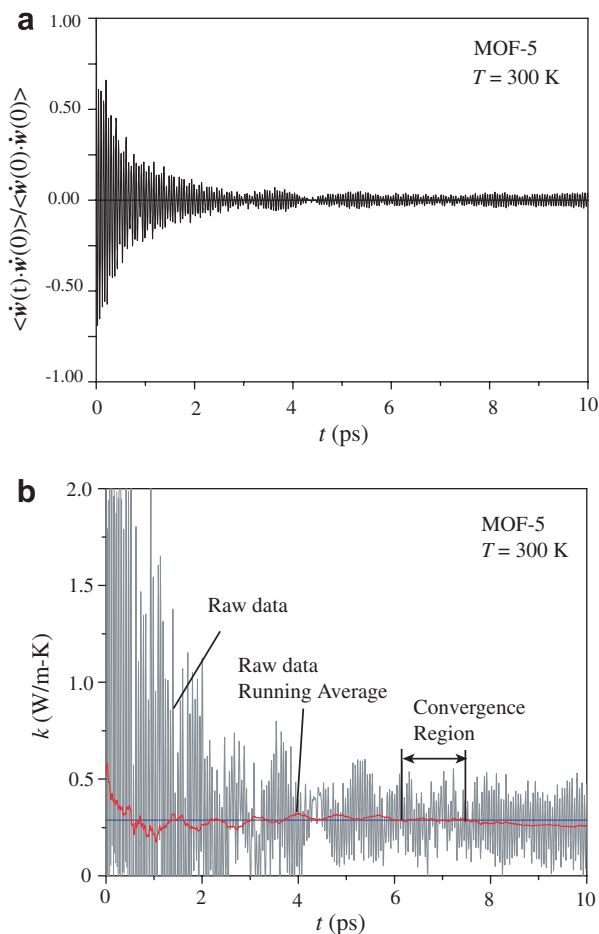
Table 3
Variation of the predicted thermal conductivity of MOF-5 with respect to the simulation system size (number of cells and total number of atoms) and temperature

T (K)	Simulation system size		
	$1 \times 1 \times 1$ (328 atoms)	$2 \times 2 \times 2$ (2624 atoms)	$3 \times 3 \times 3$ (8856 atoms)
k (W/m K)			
200	0.187 ± 0.025 (3)	0.287 ± 0.041 (3)	
250	0.197 ± 0.013 (3)	0.293 ± 0.027 (3)	
300	0.195 ± 0.007 (3)	0.308 ± 0.024 (4)	0.288 ± 0.044 (1)
350	0.205 ± 0.008 (3)	0.316 ± 0.016 (3)	0.291 ± 0.052 (1)
400	0.196 ± 0.008 (3)	0.317 ± 0.018 (3)	

The number in the parentheses is the number of simulation runs and averaged to get the reported value and the uncertainty. The uncertainty for the $3 \times 3 \times 3$ system are estimated from the fluctuation of the HCACF in the converged region of the integral.

allowing a convergence region to be defined. The decay of the normalized HCACF at a temperature of 300 K is shown in Fig. 4a, and its integral, the thermal conductivity, is shown in Fig. 4b. The HCACF vanishes after 6 ps. The MOF-5 HCACF has high frequency oscillations, believed to be related to optical phonons [32].

3.4. Simulation-size effects

In a small simulation cell, there may not be enough phonon modes to establish scattering and transport representative of the associated bulk system [34]. Such size effects will lead to a thermal conductivity different from the infinite size (bulk) limit [29,30]. The MD predicted thermal conductivities of MOF-5 are shown in Table 3, for simulation systems containing $1 \times 1 \times 1$, $2 \times 2 \times 2$ and $3 \times 3 \times 3$ unit cells (328, 2624, and 8856 atoms). The thermal conductivity of the $1 \times 1 \times 1$ system is lower than that of the larger systems. The predictions for the $2 \times 2 \times 2$ system are very close to those for the $3 \times 3 \times 3$ system at temperatures of 300 K and 350 K, indicating that the $2 \times 2 \times 2$ system will suffice to give a converged value.

4. Numerical results and analysis

4.1. Thermal conductivity and temperature dependence

The $2 \times 2 \times 2$ data from Table 3 are plotted in Fig. 5. Also included in the plot are the thermal conductivity models of Slack [24] and Cahill and Pohl [35].

Slack proposed that the thermal conductivity of crystals at temperatures above that of the experimental peak value can be approximated by the relation [36,24]

$$k_S = \frac{3.0 \times 10^4 \langle M \rangle T_D^3}{T n^{1/3} \gamma_G^2 N_c^{2/3}}, \tag{10}$$

where $\langle M \rangle$ is the mean atomic weight of the atoms in the unit cell (kg/kmol) and γ_G is the mode-averaged Grüneisen constant. This relation indicates that the thermal conductivity

Fig. 4. (a) Decay of the normalized HCACF for MOF-5 and (b) its integral (the thermal conductivity) at a temperature of 300 K.
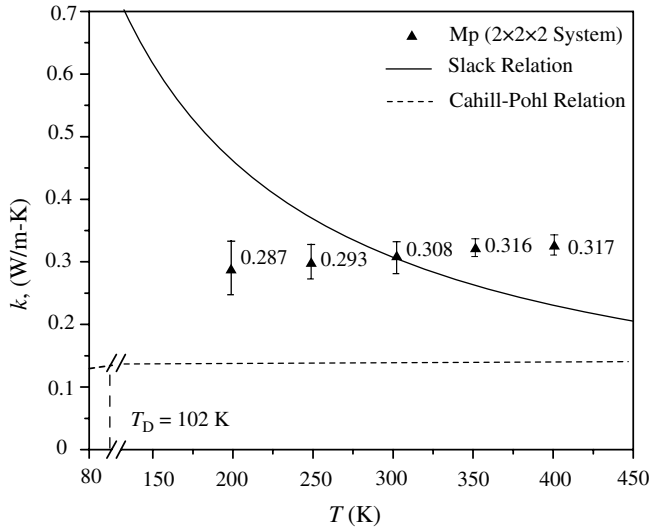
Fig. 5. Temperature dependence of the thermal conductivity of MOF-5 predicted by MD. The Slack relation [Eq. (10)], using $\gamma_G = 0.45$ to fit the predicted thermal conductivity value at $T = 300$ K and the Cahill–Pohl relation [Eq. (11)], using the MD predicted sound speeds are also shown.

will decrease with increasing temperature as T^{-1} (other factors such as γ_G have a weak temperature dependence [36]), a prediction consistent with experimental data for many crystals [36]. The decrease in the thermal conductivity is a result of a decrease in the phonon mean-free path due to an increase in inter-phonon scattering, which itself is a result of the increasing anharmonicity brought about by the higher temperatures [37,38]. The Slack model is plotted in Fig. 5 by fitting γ_G to the MD predicted thermal conductivity at a temperature of 300 K. The resulting value of γ_G is 0.45, lower than typical values between unity and two. The fit is primarily intended to allow for comparison between the trend of the Slack model and the MD data, and not as a prediction of γ_G.

Cahill and Pohl [35] developed a model for the thermal conductivity of amorphous materials by assuming that energy transfer only occurs between neighboring vibrational entities, so that the mean free path of all phonons is equal to one half of their wavelength. The thermal conductivity in this model is given by

$$k_{CP} = \left(\frac{\pi}{6}\right)^{1/3} k_B n^{2/3} \sum_{i=1}^{3} u_{p,g,i} \left(\frac{T}{T_{D,i}}\right)^2 \int_0^{T_{D,i}/T} \frac{x^3 e^x}{(e^x - 1)^2} \, dx, \tag{11}$$

and has been interpreted as a minimum solid phase thermal conductivity [24]. It is plotted in Fig. 4. The summation in the expression for k_{CP} is over the three vibration polarizations. The thermal conductivity predicted by Eq. (11) increases with increasing temperature, as more phonons modes are excited (a quantum effect, related to the specific heat). When $T \gg T_D$, Eq. (11) reaches its classical limit,

$$k_{CP,classical} = \frac{1}{2} \left(\frac{\pi}{6}\right)^{1/3} k_B n^{2/3} \sum_{i=1}^{3} u_{p,g,i}. \tag{12}$$

The thermal conductivity of MOF-5 from MD simulation at a temperature of 300 K is 0.31 ± 0.02 W/m K, a very low value for a crystal. This value can be compared with the thermal conductivities of other nanoporous crystals, such as MD predictions for the zeolites sodalite (3.5 W/m K), faujasite (2.1 W/m K), and zeolite-A (1.7 W/m K) [32], and experimental results for Tl_9BiTe_6 (0.39 W/m K) [39] and amorphous silica (1.4 W/m K) [40].

The thermal conductivity of MOF-5 according to MD simulations is almost temperature independent. A power-law fit ($k \propto T^\xi$) yields a ξ value of 0.16, different from the T^{-1} high temperature dependence predicted by Eq. (10) and kinetic theory [36]. The behavior is more similar to that of an amorphous material. This result suggests that in the temperature range of 200 K to 400 K, the mean free path of most phonons in MOF-5 has been minimized. The quantitative difference between the MD prediction and the CP model will be discussed in the next section.

4.2. Thermal conductivity decomposition

A two-stage monotonic decay of the HCACF has been reported for crystals with a one-atom unit cell [41,42]. In crystals with larger unit cells, optical phonons have been found to add high-frequency oscillations to the HCACF [32]. As such, we can decompose the HCACF of a crystal with a multi-atom unit cell into three parts [acoustic short-range (A,sh), acoustic long-range (A,lg), and optical (O)] as [32]

$$\frac{\langle \dot{\mathbf{w}}(t) \cdot \dot{\mathbf{w}}(0) \rangle}{3} = A_{A,sh} \exp(-t/\tau_{A,sh}) + A_{A,lg} \exp(-t/\tau_{A,lg}) + \sum_i B_{O,i} \exp(-t/\tau_{O,i}) \cos(\omega_{O,i} t). \tag{13}$$

The coefficients A and B represent the strength of a given mode. The summation in the optical term corresponds to a sum over the peaks in the frequency spectrum of the HCACF [32]. Then, from Eq. (8), the thermal conductivity can be decomposed into three parts as

$$k = \frac{1}{k_B V T^2} \left(A_{p,sh} \tau_{p,sh} + A_{p,lg} \tau_{p,lg} + \sum_i \frac{B_{O,i} \tau_{O,i}}{1 + \tau_{O,i}^2 \omega_{O,i}^2} \right)$$
$$\equiv k_{p,sh} + k_{p,lg} + k_O. \tag{14}$$

We first identify the optical phonon parameters by fitting to the Fourier transform of the HCACF. The resulting k_O values for the three simulation runs are then averaged. The fit optical component of the HCACF is then subtracted from the raw HCACF. The resultant HCACFs for the three simulation runs are then averaged and integrated, and the acoustic components are obtained by fitting the integral. The results for the decomposition of MOF-5 are listed in Table 4 for all the temperatures considered, and are plotted in Fig. 6. By comparing with Table 3, we see that the decomposition predicts a total thermal conductivity within 5% of the value obtained from the direct integration method. Note that k_O contributes significantly to

Table 4
Thermal conductivity decomposition for MOF-5 and the temperature dependence of the components

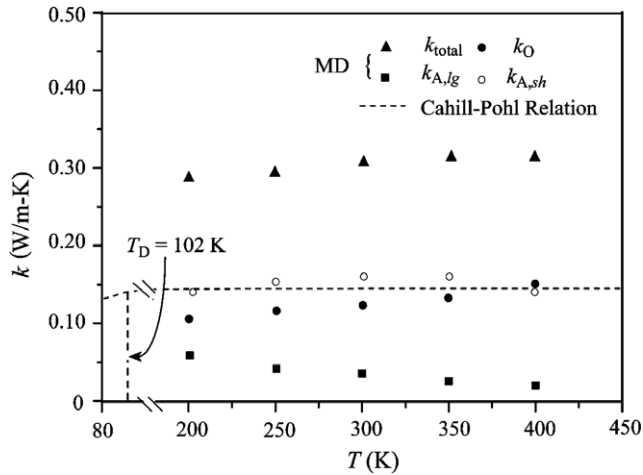| T (K)	k (W/m K)	$k_{A,lg}$ (W/m K)	$k_{A,sh}$ (W/m K)	k_O (W/m K)
200	0.298	0.051	0.141	0.106
250	0.306	0.042	0.151	0.113
300	0.305	0.029	0.160	0.116
350	0.314	0.025	0.161	0.128
400	0.318	0.021	0.142	0.155
$\xi_i (k_i \propto T^{\xi_i})$	0.09	−1.30	0.06	0.54

Fig. 6. Variation of the thermal conductivity components of MOF-5 with respect to temperature and the Cahill–Pohl relation [Eq. (11)]. The Cahill–Pohl relation uses the temperature-independent sound speeds obtained in Section 3.2.

the thermal conductivity. This contribution is often ignored in modelling efforts due to the flatness of the associated phonon dispersion branches [9,10,37]. Such an assumption is justified for materials with a large thermal conductivity [32]. For a crystal with a low thermal conductivity, such as MOF-5, the optical phonon contribution cannot be ignored. A similar result was found for silica structures [32].

The components of the thermal conductivity have different temperature dependencies: $k_{A,sh}$ is almost temperature independent ($\xi = 0.06$), and is close to k_{CP} at all temperatures (as was found for a series of silica structures [32]); k_O increases when the temperature increases ($\xi = 0.54$), and $k_{A,lg}$ decreases noticeably with increasing temperature ($\xi = −1.30$). Note that only $k_{A,lg}$ varies with temperature approximately as T^{-1}. For MOF-5, a crystal with a low thermal conductivity, the relative contribution of the long-range acoustic phonons is small and the temperature dependence of the total thermal conductivity is thus weak. Only for those crystals in which long-range correlations dominate the heat transfer (e.g., diamond, NaCl) will the total thermal conductivity vary as T^{-1}.

To develop a theoretical description of the acoustic portion of Eq. (14) ($k_A \equiv k_{A,sh} + k_{A,lg}$), we begin from the

kinetic theory for thermal conductivity and write the thermal conductivity as summation of the contributions from all phonon modes [38]

$$k = \frac{1}{3} c_v u_{p,g} \lambda_p = \sum_\kappa \frac{1}{3} c_{v,\kappa} u_{p,g,\kappa} \lambda_{p,\kappa}$$
$$= \sum_{\kappa,A} \frac{1}{3} c_{v,\kappa} u_{p,g,\kappa} \lambda_{p,\kappa} + \sum_{\kappa,O} \frac{1}{3} c_{v,\kappa} u_{p,g,\kappa} \lambda_{p,\kappa} = k_A + k_O, \quad (15)$$

where c_v is the volumetric specific heat, λ_p is the phonon mean free path, and $c_{v,\kappa}$, $u_{p,g,\kappa}$, and $\lambda_{p,\kappa}$ are the mode specific heat capacity, group velocity, and mean free path, respectively. Under the Debye approximation, the contribution of the acoustic phonons modes, k_A, can be written as [10]

$$k_A = k_B n \sum_{i=1}^{3} u_{p,g,i} \left(\frac{T}{T_{D,i}}\right)^3 \int_0^{T_{D,i}/T} \frac{x^4 e^x}{(e^x - 1)^2} \lambda_{p,i}(x) dx, \quad (16)$$

where the summation is over the three polarization branches, x is $\hbar\omega/k_B T$ and $T_{D,i}$ is $\hbar\omega_{D,i}/k_B$ ($\omega_{D,i}$ is the Debye frequency for the ith branch). In general, the mean free path is limited by boundary scattering, impurity scattering, and interphonon scattering [10,37]. At high temperatures, interphonon scattering dominates. In the MD simulations performed here, only interphonon scattering is present. To be physically meaningful, the mean free path of a phonon mode should be longer than one half of its wavelength [35]. Starting from this idea, we construct a two-segment mean free path model. When the phonon frequency is below a critical frequency, ω_c, its mean free path will vary according to the relaxation time model of Roufosse for moderate and high temperatures (above T_D) [37,43]. When the phonon frequency is above the critical frequency, its mean free path is set to one half of its wavelength. Thus, we get

$$\lambda_{p,i}(\omega) = \frac{u_{p,g,i}}{A_i(1 + B_i\omega^2)\omega^2 T}, \quad \omega < \omega_{c,i},$$
$$= \frac{\pi u_{p,g,i}}{\omega}, \quad \omega_{c,i} \leqslant \omega \leqslant \omega_{D,i},$$
$$A_i = \frac{3 \times 10^3 N_A \pi a \gamma_G^2 k_B}{2^{1/2} \langle M \rangle u_{p,g,i}^3}, \quad B_i = \left(\frac{4\pi}{3}\right)^{2/3} \frac{5a^2}{12\pi^2 u_{p,g,i}^2}, \quad (17)$$

where a is the mean interatomic distance ($a = n^{-1/3}$) and N_A is the Avogadro number. To ensure a continuous $\lambda_{p,i}(\omega)$, ω_c must satisfy

$$\omega_{c,i} A_i (1 + B_i \omega_{c,i}^2) = \frac{1}{\pi T}. \quad (18)$$

For $B_i \ll \pi^2 A_i^2 T^2$, we have

$$\omega_{c,i} \simeq \frac{1}{A_i \pi T}. \quad (19)$$

For MOF-5 at a temperature of 300 K and using $u_{p,A} = 1184$ m/s as calculated from Eqs. (6) and (7), B is 9.2×10^{-27} s^2, and $\pi^2 A^2 T^2$ is 2.1×10^{-25} s^2, so that the use of Eq. (19) is justified. At this temperature, ω_c is

2.2 Trad/s, much less than the Debye frequency ($\omega_D = 13.4$ Trad/s), indicating that most acoustic phonons have the minimum mean free path.

The critical frequency ω_c decreases with temperature (for MOF-5, ω_c at temperatures of 200 K, 250 K, 300 K, 350 K, and 400 K is 3.3 Trad/s, 2.6 Trad/s, 2.2 Trad/s, 1.9 Trad/s, and 1.7 Trad/s). That is, as the temperature increases, an increasing number of phonon modes reach the limiting mean free path of one half of their wavelength. Using Eq. (17), Eq. (16) can be rewritten as

$$k_A = \sum_{i=1}^{3} \frac{k_B}{2\pi^2 u_{p,g,i} A_i T} \int_0^{\omega_{c,i}} \left[\left(\frac{4\pi}{3}\right)^{2/3} \frac{5\omega^2 a^2}{12\pi^2 u_{p,g,i}^2} + 1 \right]^{-1} d\omega$$

$$+ \left(\frac{\pi}{6}\right)^{1/3} n^{2/3} \sum_{i=1}^{3} u_{p,g,i} \frac{\hbar^4}{T_{D,i}^2 k_B^3 T^2} \int_{\omega_{c,i}}^{k_B T_{D,i}/\hbar} \frac{\omega^3 e^{\frac{\hbar\omega}{k_B T}}}{(e^{\frac{\hbar\omega}{k_B T}} - 1)^2} d\omega. \tag{20}$$

Based on the construction of this model, and our knowledge of the GK thermal conductivity decomposition, we associate the first term in Eq. (20) with $k_{A,lg}$ and the second term with $k_{A,sh}$. In considering Eq. (20), even if the temperature dependencies of the material properties and phonon dispersion are ignored, $k_{A,lg}$ still departs from T^{-1} behavior (T^ξ with $\xi < -1$). This is because ω_c decreases with temperature. At the same time, $k_{A,sh}$ increases slightly with temperature and eventually saturates. The lower ω_c, the larger the fraction of $k_{A,sh}$ in k_A. Eq. (20) also predicts that the temperature dependence of k_A will become progressively weaker as temperature increases.

In Fig. 7, the temperature dependencies of $k_{A,lg}$ and $k_{A,sh}$ predicted by the two-stage model are shown along with the MD decomposition data. The $k_{A,lg}$ component is fit to the decomposition data at 300 K by setting γ_G equal to 1.0. As with the fit to the Slack model in Fig. 5, the purpose of the fit is to compare the general trends, and not to specify γ_G. The agreement between the trends in the model and the MD data are good. Note that the thermal conductivity predicted by Eq. (20) goes to infinity as the temperature goes to zero, typical of a crystal in an MD simulation, where there are no quantum effects. A simulation of MOF-5 at a temperature of 50 K (lower than T_D) gives a thermal conductivity of 2.8 W/m K, consistent with this trend. While this numerical value cannot be compared with the experiments due to the exclusion of quantum effects (phonon excitation), it does indicate that MOF-5 behaves like a crystal in the simulations (the thermal conductivity of amorphous materials in MD decreases as the temperature decreases, consistent with experimental data [33,44,32]).

By setting ω_c equal to ω_D, $u_{p,g,i}$ to the mean phonon speed $u_{p,g}$, and using $\omega_D = u_{p,g}(6\pi^2 n/N_c)^{1/3}$, we have, from Eq. (20),

$$k = k_{A,lg} = \frac{4.48 \times 10^3 \langle M \rangle T_D^3}{T n^{1/3} \gamma_G^2 N_c^{2/3}}, \tag{21}$$

which is similar to the Slack relation (Eq. (10)), except for the constant. The difference in the constants is due to the single-mode relaxation time approximation and a different Hamiltonian used by Roufosse for three-phonon interactions [37]. If ω_c is equal to zero, only $k_{A,sh}$ contributes to k_A, and as expected, Eq. (20) reduces to Eq. (11). For $T/T_{D,i} \gg 1$, ω_c vanishes, and k_A will reach the classical limit of k_{CP}, Eq. (12).

Since $k_{A,sh}$ and k_O are small and their temperature dependencies are not strong (their sum has been interpreted as a thermal conductivity limit in crystals [32]), we may obtain a crystal with a low thermal conductivity and a weak temperature dependence by reducing ω_c. This can be accomplished by reducing the sound speed and increasing the mean interatomic distance.

4.3. Examination of vibrations

The thermal conductivity of a dielectric material is related to the lattice vibrations (i.e., phonon transport). To further investigate the low thermal conductivity of MOF-5, we will calculate the partial density of states (PDOS) of the distinct atomic positions in the unit cell. The PDOS of the βth species, $D_{p,\beta}$, is determined by taking the Fourier transform of the velocity auto-correlation function, and weighting the result with the species concentration c_β [45]:

$$D_{p,\beta}(\omega) = c_\beta \int_0^\tau \Gamma_\beta(t) \cos(\omega t) dt, \tag{22}$$

where

$$\Gamma_\beta(t) = \sum_{i}^{N_\beta} \langle \mathbf{u}_{i\beta}(t) \cdot \mathbf{u}_{i\beta}(0) \rangle / \sum_{i}^{N_\beta} \langle \mathbf{u}_{i\beta}(0) \cdot \mathbf{u}_{i\beta}(0) \rangle. \tag{23}$$
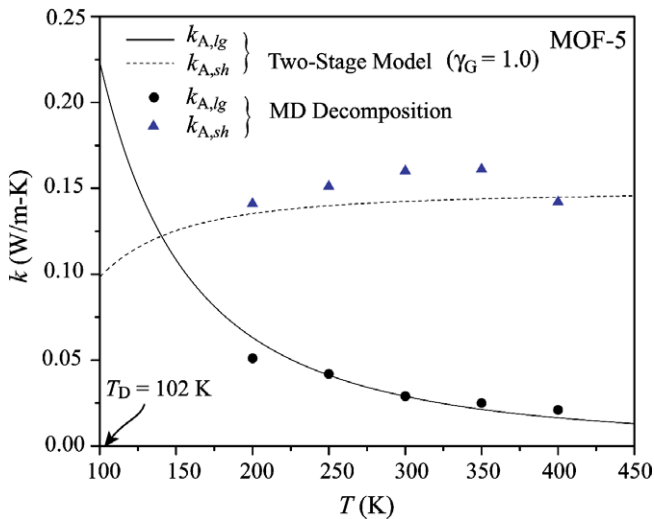

Fig. 7. The variation of $k_{A,lg}$ and $k_{A,sh}$ with respect to temperature predicted by the two-stage model and from the MD decomposition. The longitudinal and transverse sound speeds are taken to be 1672 m/s and 1033 m/s (see Section 3.2), and γ_G is set as 1.01 to fit $k_{A,lg}$ at a temperature of 300 K.

The total phonon DOS is obtained by summing over the partial DOS:

$$D_p(\omega) = \sum_\beta D_{p,\beta}(\omega). \tag{24}$$

The PDOS indicates the vibrational modes that specific atoms are involved with in the overall crystal lattice dynamics. In a classical system, such as an MD simulation, and in real systems well above the Debye temperature, all degrees of freedom have approximately the same expectation value for their energy. Thus, one can interpret the area under the PDOS curves as an indication of how the system energy is distributed among the atoms.

In Fig. 8a, two cages and one bridge of the MOF-5 structure are shown, and the arrows are used to illustrate the transport of vibrations from the atom C1. In Figs. 8b and 8c, the PDOS of the Oc, Zn, O, C1, C2, and C3 atoms are plotted. The C1 and C2 atoms have the same PDOS. Motivated by the decomposition of the thermal conductivity, we can examine the vibrations in both the low- and high-frequency regimes.

In the acoustic phonon modes, which end around 14 Trad/s (2.3 THz), the center oxygen atom (Oc) essentially doesn't participate. If one thinks of the heat transfer as energy moving from atom to atom, in the cage structure it will need to take a circuitous route around the Oc atom.

There is also more activity in the C3 (which are a part of the phenylene ring) and O1 (which are a part of the cage) atoms than the C1/C2 atoms. The C1/C2 atoms act as a bottleneck. We interpret this result as a sign of energy localization. The phenylene ring can pivot about the axis defined by the C1–C2 bond, and yet these motions are difficult to pass onto the cage and vice versa. Energy moves back and forth across the bridge, or inside the cage, as it is reflected at the connection between them. In this way, the development of long-range correlations is suppressed. A similar trend is observed in the optical phonon spectrum of the C3 atoms. There is also scant overlap between the PDOS of the Zn and O atoms at the higher frequencies (most likely brought about by their mass difference), identifying another point in the structure where transmitting energy will be difficult. The overall picture is thus one of cages and bridges between which energy flow is restricted. This is a finding similar to that for zeolites [32], where energy localization on specific Si–O–Si structures was identified.

5. Summary

We have developed a set of optimized classical interatomic potentials for MOFs and used them to predict the thermal conductivity of MOF-5 between temperatures of
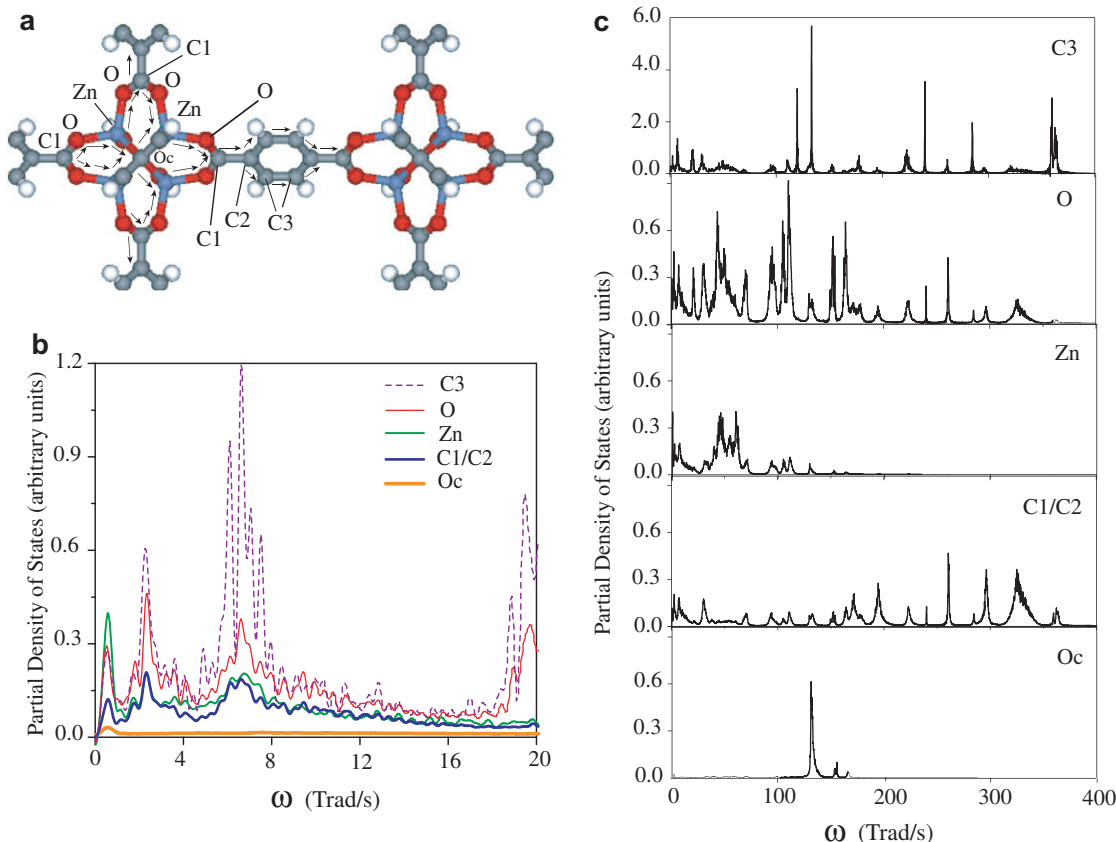

Fig. 8. (a) Section of the MOF-5 structure. (b) and (c) PDOS of Oc, Zn, O, C1, C2, and C3 atoms in the simulation cell. Note that the scale for the C3 atoms is different than the others in (c).

200 K and 400 K using MD simulations and the GK method. The thermal conductivity of MOF-5 is low (0.31 W/m K at a temperature of 300 K) and shows a weak temperature dependence, very different from the $k \propto T^{-1}$ behavior exhibited by many crystals at high temperature, but similar to the behavior of amorphous phases.

The thermal conductivity of MOF-5 can be decomposed into three parts: the acoustic short-range, acoustic long-range and optical contributions, as shown in Table 4 and Fig. 6. The decomposition indicates that the short-range acoustic phonons and the optical phonons dominate the energy transport. The long-range acoustic phonons contribute little to the total thermal conductivity, resulting in an amorphous-like behavior at high temperatures. We believe this to be a common characteristic for nanoporous crystals with a low thermal conductivity.

We developed Eq. (20), which is based on a two-stage mean free path, to explain the acoustic portion of the decomposition. The short-range contribution ($k_{A,sh}$) is found to be related to phonons that have mean free paths equal to one half of their wavelengths, and the long-range contribution ($k_{A,lg}$) to phonons with longer mean free paths. A critical frequency (ω_c) has been defined, which indicates the relative contributions of the short and long-range acoustic phonons. When ω_c is small the short-range component dominates the thermal transport, and the acoustic contribution to the thermal conductivity reaches the CP limit. When ω_c is large, the long-range phonons dominate, and the total thermal conductivity varies approximately as T^{-1}.

To summarize, we can explain the low thermal conductivity of MOF-5 using the simple kinetic relation $k = c_v u_{p,g} \lambda_p / 3$ (Eq. (15)). The open structure of MOF-5 results in a low atomic number density and leads to a low c_v, and the long, flexible bridge and the heavy cage cluster result in a low phonon group velocity. The cage-bridge structure suppresses the development of long range correlations and reduces the phonon mean free path. While the results presented are specific to MOF-5, the general findings are applicable to other MOFs. With MD as a tool, and the MOF family of materials to work with, the design of new, highly insulating materials appears to be a realistic goal.

Acknowledgements

References

[1] H. Lir, M. Eddaoudi, M. O'Keeffe, O.M. Yaghi, Design and synthesis of an exceptionally stable and highly porous metal-organic framework, Nature 402 (1999) 276.

[2] M. Eddaoudi, J. Kim, N. Rosi, D. Vodak, J. Wachter, M. O'Keeffe, O.M. Yaghi, Systematic design of pore size and functionality in isoreticular mofs and their application in methane storage, Science 295 (2002) 469.

[3] O.M. Yaghi, M. O'Keeffe, N.W. Ockwig, H.K. Chae, M. Eddaoudi, J. Kim, Reticular synthesis and the design of new materials, Nature 423 (2003) 705.

[4] J.L.C. Rowsell, O.M. Yaghi, Metal-organic frameworks: a new class of porous materials, Micropor. Mesopo. Mater. 73 (2004) 3.

[5] N.L. Rosi, J. Eckert, M. Eddaoudi, D.T. Vodak, J. Kim, M. O'Keeffe, O.M. Yaghi, Hydrogen storage in microporous metal-organic frameworks, Science 300 (2003) 1127.

[6] J.L.C. Rowsell, A.R. Millward, K.S. Park, O.M. Yaghi, Hydrogen sorption in functionalized metal-organic frameworks, J. Am. Chem. Soc. 126 (2004) 5666.

[7] J.L.C. Rowsell, E.C. Spencer, J. Eckert, J.A.K. Howard, O.M. Yaghi, Gas adsorption sites in a large-pore metal-organic framework, Science 309 (2005) 1350.

[8] A.I. Skoulidas, D.S. Sholl, Self-diffusion and transport diffusion of light gases in metal-organic framework materials assessed using molecular dynamics simulations, J. Phys. Chem. B 109 (2005) 15760.

[9] J. Callaway, Model for lattice thermal conductivity at low temperatures, Phys. Rev. 113 (1959) 1046–1051.

[10] M.G. Holland, Analysis of lattice thermal conductivity, Phys. Rev. 132 (1963) 2461.

[11] A.J.H. McGaughey, M. Kaviany, Quantitative validation of the boltzmann transport equation phonon thermal conductivity model under the single-mode relaxation time approximation, Phys. Rev. B 69 (2004) 094303.

[12] R.W. Grimes, D.J. Binks, A.B. Lidiard, The extent of zinc-oxide solution in zinc chromate spinel, Philos. Mag. A 72 (1995) 650–668.

[13] M.J. Frisch et al., Gaussian 98 (Revision A.11), Gaussian, Inc, Pittsburgh PA, 2001.

[14] J.D. Gale, A.L. Rohl, The general utility lattice program (gulp), Mol. Simulat. 29 (2003) 291–341.

[15] R. Chelli, G. Cardini, P. Procacci, R. Righini, S. Califano, A. Albrecht, Simulated structure, dynamics, and vibrational spectra of liquid benzene, J. Chem. Phys. 113 (2000) 6851.

[16] A.R. Leach, Molecular Modelling Principles and Applications, Addison Wesley Longman Ltd., Reading, MA, 1996.

[17] Z. Ni, Chemistry Department, University of Michigan, personal communication.

[18] B. Boulard, J. Kieffer, C.C. Phifer, C.A. Angell, Vibrational-spectra in fluoride-crystals and glasses at normal and high-pressures by computer-simulation, J. Non-Cryst. Solids 140 (1992) 350.

[19] J. Sauer, J. Dobler, Gas-phase infrared spectrum of the protonated water dimer: Molecular dynamics simulation and accuracy of the potential energy surface, ChemPhysChem 6 (2005) 1706–1710.

[20] D. Wolf, P. Keblinski, S.R. Phillpot, J. Eggebrecht, Exact method for the simulation of coulombic systems by spherically truncated, pairwise r(-1) summation, J. Chem. Phys. 110 (1999) 8254.

[21] P. Demontis, S. Spanu, G.B. Suffritti, Application of the wolf method for the evaluation of coulombic interactions to complex condensed matter systems: aluminosilicates and water, J. Chem. Phys. 114 (2001) 7980–7988.

[22] D. Frenkel, B. Smit, Understanding Molecular Simulation: From Algorithms to Applications, Academic Press, San Diego, 1996.

[23] C. Kittel, Introduction to Solid State Phys., Wiley Inc, New York, 1996.

[24] G.A. Slack, Solid State Phys. 34 (1979).

[25] J.M. Haile, Molecular Dynamics Simulation Elementary Methods, Wiley Inc, New York, 1992.

[26] M.T. Dove, Introduction to Lattice Dynamics, Cambridge University Press, Cambridge, 1993.

[27] A.D. Nashif, D.I.G. Jones, J.P. Henderson, Vibration Damping, Wiley, New York, 1985.

[28] D.A. McQuarrie, Statistical Mechanics, University Science Books, Sausalito, 2000.

[29] J. Che, T. Cagin, W. Deng, W.A. Goddard, Thermal conductivity of diamond and related materials from molecular dynamics simulations, J. Chem. Phys. 113 (2000) 68888.

[30] P.K. Schelling, S.R. Phillpot, P. Keblinski, Comparison of atomic-level simulation methods for computing thermal conductivity, Phys. Rev. B 65 (2002) 144306.

[31] S.G. Volz, G. Chen, Molecular-dynamics simulation of thermal conductivity of silicon crystals, Phys. Rev. B 61 (2000) 2651.

[32] A.J.H. McGaughey, M. Kaviany, Thermal conductivity decomposition and analysis using molecular dynamics simulations – part ii. complex silica structures, Int. J. Heat Mass Transfer 47 (2004) 1799.

[33] Y.H. Lee, R. Biswas, C.M. Soukoulis, C.Z. Wang, C.T. Chan, K.M. Ho, Molecular-dynamics simulation of thermal-conductivity in amorphous-silicon, Phys. Rev. B 43 (1991) 6573.

[34] A.J.H. McGaughey, M. Kaviany, Observation and description of phonon interactions in molecular dynamics simulations, Phys. Rev. B 71 (2005) 184305.

[35] D.G. Cahill, S.K. Watson, R.O. Pohl, Lower limit to the thermal-conductivity of disordered crystals, Phys. Rev. B 46 (1992) 6131.

[36] R. Berman, Thermal Conduction in Solids, Clarendon Press, Oxford, 1976.

[37] M. Roufosse, P.G. Klemens, Thermal-conductivity of complex dielectric crystals, Phys. Rev. B 7 (1973) 5379.

[38] G.P. Srivastava, The Physics of Phonons, Adam Hilger, New York, 1990.

[39] B. Wolfing, C. Kloc, J. Teubner, E. Bucher, High performance thermoelectric tl9bite6 with an extremely low thermal conductivity, Phys. Rev. Lett. 86 (2001) 19.

[40] Y. Touloukian, Thermalphysical Properties of Matter, Plenum, New York, 1970.

[41] A.J.H. McGaughey, M. Kaviany, Thermal conductivity decomposition and analysis using molecular dynamics simulations. part i. lennard-jones argon, Int. J. Heat Mass Transfer 47 (2004) 1783–1798.

[42] J. Li, L. Porter, S. Yip, Atomistic modeling of finite-temperature properties of crystalline beta-sic – ii. Thermal conductivity and effects of point defects, J. Nucl. Mater. 255 (1998) 139–152.

[43] V.A. Konstantinov, Manifestation of the lower limit to thermal conductivity in the solidified inert gases, J. Low Temp. Phys. 122 (2001) 459.

[44] P. Jund, R. Jullien, Molecular-dynamics calculation of the thermal conductivity of vitreous silica, Phys. Rev. B 59 (1999) 13707.

[45] C.-K. Loong, Phonon density of states and oxygen-isotope effect in ba1-xkxbio3, Phys. Rev. B 45 (1992) 8052.